Nano Research
2023, 16(2): 2035–2040

ISSN 1998-0124 CN 11-5974/O4
https://doi.org/10.1007/s12274-022-4868-3

Research Article

Ultra-stable Pt_5La intermetallic compound towards highly efficient oxygen reduction reaction

Siyuan Zhu[1,2], Liting Yang[1,2], Jingsen Bai[1,2], Yuyi Chu[1,2], Jie Liu[1,2], Zhao Jin[1,2], Changpeng Liu[1,2], Junjie Ge[1,2,3] (), and Wei Xing[1,2] ()

[1] *State Key Laboratory of Electroanalytical Chemistry, Laboratory of Advanced Power Sources, Changchun Institute of Applied Chemistry, Chinese Academy of Sciences, Changchun 130022, China*
[2] *School of Applied Chemistry and Engineering, University of Science and Technology of China, University of Science and Technology of China (USTC), Hefei 230026, China*
[3] *Dalian National Laboratory for Clean Energy, Chinese Academy of Sciences, Dalian 116023, China*

Received: 10 June 2022 / **Revised:** 26 July 2022 / **Accepted:** 4 August 2022

ABSTRACT

Designing feasible electrocatalysts towards oxygen reduction reaction (ORR) requires advancement in both activity and stability, where attaining high stability is of extreme importance as the catalysts are expected to work efficiently under frequent start-up/shut down circumstances for at least several thousand hours. Alloying platinum with early transition metals (i.e., Pt–La alloy) is revealed as efficient catalysts construction strategy to potentially satisfy these demands. Here we report a Pt_5La intermetallic compound synthesized by a novel and facile strategy. Due to the strong electronic interactions between Pt and La, the resultant Pt_5La alloy catalyst exhibits enhanced activity with half wave of 0.92 V and mass activity of 0.49 $A \cdot mg_{Pt}^{-1}$, which strictly follows the 4e transfer pathway. More importantly, the catalyst performs superior stability during 30,000 cycles of accelerated stressed test (AST) with mass activity retention of 93.9%. This study provides new opportunities for future applications of Pt-rare earth metal alloy with excellent electrocatalytic properties.

KEYWORDS

oxygen reduction reaction, intermetallic compound, rare earth metal, electrocatalysis

1 Introduction

Heavy use of scarce platinum as the cathode catalyst is a central constraint to the widespread deployment and commercialization of proton exchange membrane fuel cells (PEMFCs) [1, 2]. During the several past decades, researchers have been continuously working on lowering the Pt loading on the electrodes to counter balance the high price and scarcity of platinum and thereby ensure a sustainable future. The endeavors include efforts in both enhancing Pt utilization efficiency by increasing effective electrochemical area and boosting the intrinsic activity, and preferably, the combination of the two.

To achieve high performance, incorporation of second metal elements into Pt-based catalysts is generally regarded as an effective solution [3]. It is expected to optimize the catalytic performance of platinum and further reduce the amount of platinum through strong interactions between metals [4, 5]. Benefiting from regulated ligand effect and manipulable geometrical effect [6], Pt-based alloy electrocatalysts always exhibit lower overpotential and higher power density than that of pure Pt counterparts in oxygen reduction reaction (ORR). Previous literature reported manifest excellent activity of Pt alloyed with late transition metals [7–11]. However, the problem is that the late transition metals in these alloys are not immune to dissolution in harsh corrosive environments, which will seriously cause unsteady problems. First is that dealloying degradation directly reduces the available active sites, inevitably leading to performance degradation of PtM activity [1]. Secondly, the dissolved metal may further react with the by-product H_2O_2 and generates free radicals, which will attack carbon support ionomer/membrane and bipolar plate, causing uncontrollable damage to the test system [12]. In contrast, the early transition alloy metals can well avoid the above problems [13]. Theoretically speaking, the dissolution potential of the alloy is high, and the second metal is thermodynamically stable [14]. In addition, the radius of the early transition metal is large, and reasonable control of it in the subsurface layer may suppress the leaching of the second metal due to geometric obstruction [15]. In previous reports, Norskov et al. [13] already predicted the excellent stability of early transition metal alloys from theoretical level, with calculational results showed Pt_xSc and Pt_xY as the most stable Pt-based alloys.

Among the early transition metals, rare earth elements have received much attention as effective promoters due to their unique 4f shell electronic structure [16]. However, we know that because rare earth metals are chemically active and possess low reduction potentials, bulk rare earth oxides are almost the predominant promoter species present in previously reported [17]. Rare earth oxides can contribute to the electrochemical activity of catalysts to a certain extent, but they suffer from two significant disadvantages: poor electrical conductivity and obvious solubility in acidic media.

Address correspondence to Junjie Ge, gejj@ciac.ac.cn; Wei Xing, xingwei@ciac.ac.cn

To overcome these drawbacks, synthetic strategies for Pt-rare earth alloy catalysts should be explored. Until this moment, regrettably, there are few reports of feasible synthetic methods owing to the low chemical potential of early transition metals [18].

Herein, this report describes an efficient surfactant-free synthetic route for the preparation of platinum-lanthanum (Pt_5La) alloy catalysts. The Pt_5La alloy exhibits high mass activity of 0.49 $A \cdot mg_{Pt}^{-1}$ at 0.9 V and, more importantly, the high durability (< 1% loss on half potential after 30,000 cycles and < 7% loss of mass activity) under ORR operating conditions, providing the alloy material expansion with superior activity and extreme stability.

2 Result and discussion

The synthesis procedure of Pt_5La is described in Fig. 1, following an original-design synthetic pathway. And the process involves only two simple steps. First, we start from the readily available rare earth metal salts and commonly organic ligand, i.e., trimesic acid. The two precursor materials were self-assembled into rod-shaped metal–organic frameworks (MOFs) under controlled temperature and solvent, as described in the Electronic Supplementary Material (ESM). Detailed size and morphology of the nanorods are accessible in Fig. S1 in the ESM. As illustrated in Fig. 1, the as-synthesized La-MOFs are composed of groups of ligands linked to La oxides in an orderly manner. The La-MOFs were then carbonized at high temperature for *in-situ* adsorption of the Pt precursor to be introduced in the next step. And in typical step of controlling alloy formation, the nanorods impregnated with noble metal source need to undergo a high temperature annealing process. Usage of synthesis gas (10% H_2 in Ar) as reducing agent at 900 °C ensures the smooth progress of above annealing process. Briefly, we created a robust wet chemistry method to facilely obtain the Pt-rare earth alloy nanoparticles. Detailed features and morphology of prepared samples were represented by systematic characterization in Figs. 2 and 3.

In Fig. 2(a), representative scanning transmission electron microscopy (STEM) image shows a homogeneous dispersion of particles bright spots, indicating a wide range of uniformity of nanoparticles that can be clearly identified even at low magnification. The crystal structures of these nanoparticles were acquired by powder X-ray diffraction (PXRD) patterns. After careful comparison, patterns of our samples are in perfect agreement with the standard pattern of standard Pt_5La in the PDF database, so it can be considered that we have prepared Pt_5La alloy. Based on Fig. 2(b), the as-synthesized sample showed a completely different diffraction pattern from that of ordinary face-centered cubic (fcc) crystal configuration in Pt-based alloys. According to PDF No. 65-5283, the unit cell with the diffraction peaks of $a = b = 5.386$ and $c = 4.376$ Å can be indicated to a hexagonal close packed (hcp) phase [19]. The distortion of crystal configuration in alloy is attributed to the successful incorporation of rare earth atoms, which is likely to affect the subsequent catalytic performance. Also, in detail, Pt-La alloy supported on the carbon rods showed additional superlattice peaks at 19.011 and 27.934, which are characteristic of intermetallic compounds [20–22]. Subsequently, we performed high-resolution transmission electron microscopy (HR-TEM) images and corresponding selected area electron diffraction (SAED) for individual branches to obtain further structural information. Investigated data presented in Figs. 2(e) and 2(f) fully supported the successful preparation of intermetallic Pt_5La alloy with the appearance of characteristic crystal planes [14].

To verify the elemental composition of the as-prepared products, inductively coupled plasma atomic emission spectroscopy (ICP-AES) analysis for samples, energy dispersive X-ray spectroscopy (EDS) mapping under STEM for area, and line scanning for single particles were all employed. According to the structure analyzed by EDS, Pt and La atoms were uniformly distributed over the whole carbon substrate, and the STEM-EDS line-scanning intensity profile supported Pt and La metal ratio of 5:1 in the single particle. The total mass of Pt was measured by ICP-AES to be 7.0 wt.% and the total mass of La was 0.9 wt.%, respectively, which is very close to the EDS result.

Then we carried out X-ray photoelectron spectroscopy (XPS) and X-ray absorption (XAS) spectra measurements to investigate oxidation states on the surface area as well as electric charge transfer between Pt and La atoms. Figures 3(a) and 3(c) showed high-resolution XPS spectra of Pt and La. From Fig. 3(a), the Pt 4f spectrum could be decoupled as two pairs of peaks, Pt $4f_{5/2}$ and Pt $4f_{7/2}$, with the co-existence of two different valence states on the sample surface. Compared with Pt 4f spectra of Pt/C-JM presented in Fig. S3 in the ESM, the binding energy positions of deconvoluted peaks represented metallic Pt(0) and Pt(II) oxide in Pt_5La both exhibited a slight negative shift. Notably, the fractions of zero-valent Pt for Pt_5La alloy (50.5%, calculated from ratio of peak areas) are significantly higher than that of Pt/C-JM (45.8%), denoting the favorable formation of metallic Pt in Pt_5La. Simultaneously, we acquired the La 3d high-resolution XPS spectrum, with only one small peak at 859 eV, originating from the La(III) contribution. Due to the acid washing and drying process during catalyst synthesis, small amount of La atoms on the surface of the Pt_5La alloy was oxidized, resulting in a proportion of La(III) oxide states presenting on the catalytic surface. Compared to the La(III) $3d_{3/2}$ value in La-MOF shown in Fig. S4 in the ESM, La(III) $3d_{3/2}$ in Pt_5La is positively shifted. These evidences demonstrated the existence of an apparent electron donation phenomenon from less electronegative adjacent La metals to Pt metals in the bimetallic alloy nanoparticles [14].

Then we carried out X-ray absorption near-edge structure

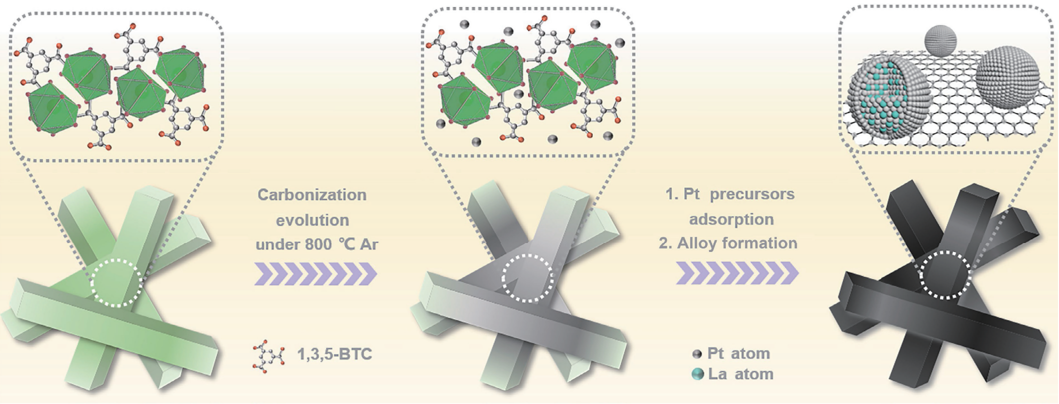

Figure 1 Schematic illustration of the synthesis procedure of La-MOF and Pt_5La alloy.

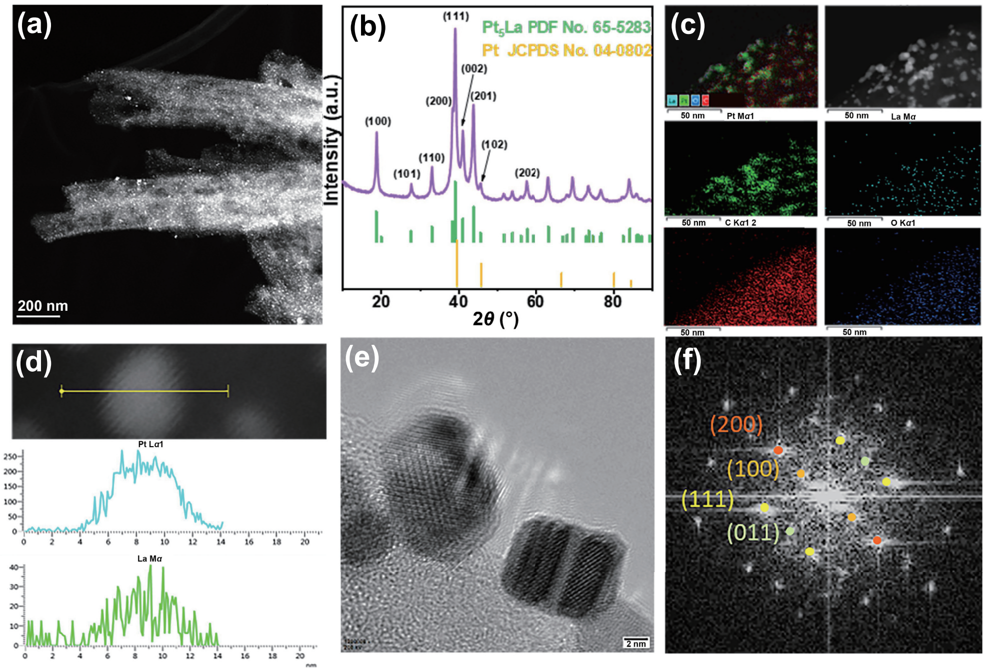

Figure 2 (a) A STEM image shows uniform alloy dispersion on the nanorods, scale bar: 200 nm. (b) XRD patterns of Pt_5La alloy and standard data from database. (c) EDS mapping of Pt, La, C, and O elements of the excavated area, scale bar: 50 nm. (d) STEM-EDS line-scanning intensity profile. (e) HR-TEM of prepared Pt_5La alloy, scale bar: 2 nm. (f) The corresponding SAED pattern taken from (e).

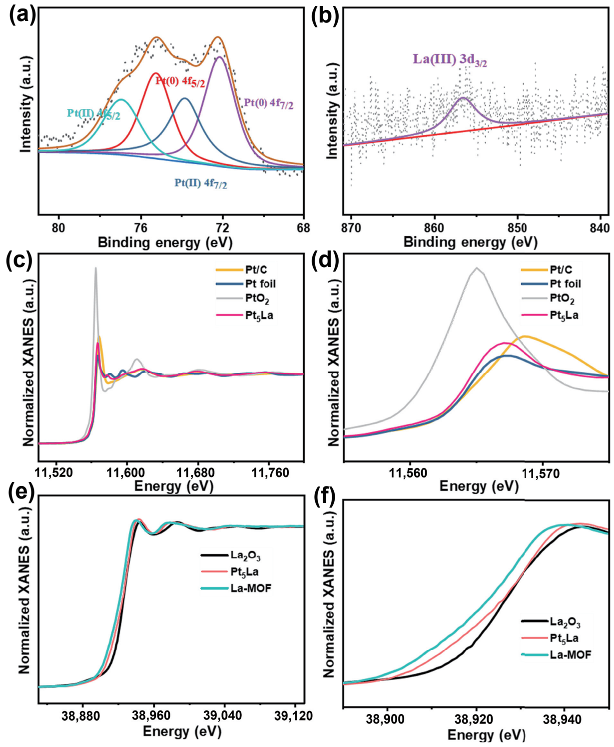

Figure 3 (a) XPS delectation of Pt 4f in Pt_5La. (b) XPS delectation of La 3d in Pt_5La. (c) XANES spectra at the Pt L_3 edge. (d) Image from partial enlarged view of (c). (e) XANES spectra at the La K edge. (f) Image from partial enlarged view of (e).

(XANES) analysis at around 30 eV near the absorption edge of Pt L_3 edge and the La K edge to determination of the local electronic of the two elements in the Pt_5La alloy. From Figs. 3(c) and 3(d), we can see that the electronic state of the intermetallic compound nanoparticles was markedly different from that of Pt/C-JM because of the shift in edge energy. Upon the formation of intermetallic compounds, the intensity of the white line in Pt_5La was close to Pt foil rather than Pt/C-JM. It indicated that Pt in Pt_5La showed the metallic state and excluded massive Pt–O bond formation, consistent with the results from XPS. Furthermore, a noticeable shift in edge energy to higher energy during the conversion from La-MOF to Pt_5La alloy from Figs. 3(e) and 3(f) confirms the electron transfer from La to Pt in the alloy particles.

To evaluate ORR performance of Pt_5La, we used cyclic voltammetry (CV) and linear scanning voltammetry (LSV) by rotating ring disk electrode tests in a three-electrode system, and the results are listed in Fig. 4. Figures 4(a) and 4(b) showed the CV curves and LSV curves of Pt_5La alloy based electrodes at a scan rate of 20 $mV{\cdot}s^{-1}$ in 0.1 M $HClO_4$ solution that were saturated in both N_2 and O_2 environment. In Fig. 4(a), the catalysts showed hydrogen adsorption/desorption characteristics, indicating the ideal exposure of the Pt surface to the reactant interface. The polarization curves in Fig. 4(b) demonstrated the excellent adsorption and reduction capacity of the Pt_5Ls alloy catalyst for oxygen, depending on the half-wave potential at 0.92 V and the limiting current close to 6 $mA{\cdot}cm^{-2}$. And the onset potential of the Pt_5La alloy can be recorded as 0.998 V, corresponding to the higher ORR activity by a positive shift of 21 mV relative to commercial Pt/C-JM. Benefiting from the great enhancement in activity, the mass activity at 0.9 V_{RHE} of 0.49 $A{\cdot}mg_{Pt}^{-1}$ for Pt_5La alloy exceeded the target of department of energy (DOE) at 0.37 $A{\cdot}mg_{Pt}^{-1}$ and is two times of that of the commercial Pt/C-JM catalyst (Fig. 4(e)). In addition, electrochemically active surface area (ECSA, normalized by mass) of Pt_5La alloy calculated from CO stripping method was 104.1 $m^2{\cdot}g^{-1}$. Compared with the ECSA of approximate 80 $m^2{\cdot}g^{-1}$ usually tested and calculated by Pt/C-JM, this superior result is attributable to the good dispersion of alloy catalysts, in line with our previous work [23].

To investigate whether the ORR pathways of our catalyst belong to the $2e^-$ transfer process with generating hydrogen peroxide or the four electron-producing hydroxyl group process, we applied a constant voltage to the ring and collected the response current. The H_2O_2 yield of the Pt_5La alloy catalyst was less than 1% from Fig. 4(f), and Fig. 4(c) further proved a four-electron reduction pathway. This avoids generation of unwanted free H_2O_2 like late transition metal alloys, which can cause oxidative obstacles to the entire test system [12].

Fuel cell performance under both H_2/O_2 and H_2/air operating

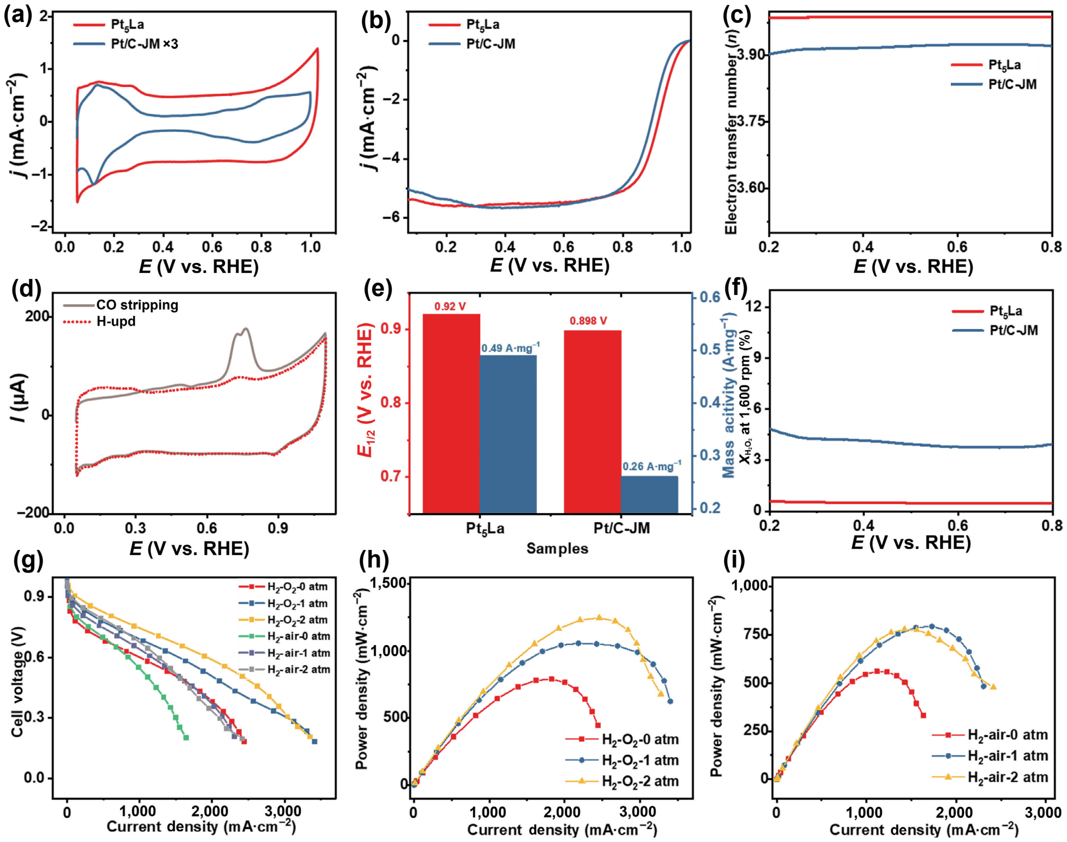

Figure 4 (a) CV curves of the Pt_5La alloy and Pt/C-JM in N_2-saturated 0.1 M $HClO_4$ at a scan rate of 20 mV·s^{-1}. (b) LSV curves of the Pt_5La alloy and Pt/C-JM in O_2-saturated 0.1 M $HClO_4$ at a scan rate of 20 mV·s^{-1}. (c) Electron transfer numbers acquired. (d) CO stripping methods for calculation of ECSA. (e) Detailed comparation of the half-wave potential and the mass activity of the catalysts at 0.9 V vs. RHE. (f) H_2O_2 yield of the Pt_5La alloy and Pt/C-JM catalysts. (g) *I*–*V* curves of Pt_5La measured with completely humid air or oxygen at different back pressure values in fuel cells. (h) Corresponding power density curves of H_2/O_2 fuel cells. (i) Corresponding power density curves of H_2/air fuel cells.

conditions was then investigated by assembling Pt_5La alloy into the membrane electrode assemblies (MEAs). Polarization curves and power density curves are presented in Figs. 4(g) and 4(h). The PEMFCs fabricated with Pt_5La catalyst showed peak power density as high as 1,247 mW·cm^{-2} in H_2/O_2 condition and 794 mW·cm^{-2} in H_2/air condition. The reproducibility of the performance from half-cell system to the MEA ensures the excellent electrocatalytic activity of the Pt_5La catalyst.

Hereafter, we exanimated the durability of Pt_5La alloy and Pt/C-JM as benchmark samples through accelerated stressed test (AST) by applying continuous potential cycling (up to 30,000 cycles) in an O_2-saturated $HClO_4$ solution at room temperature. The test potentials were set from 0.6 to 0.95 V, where Pt tends to dissolve. Figure 5 presents the changes in key electrochemical performance parameters, such as CV curves, half wave potential, and mass activity. In Fig. 5(a), we found that the LSVs recorded every 10,000 cycles are almost completely coincident, representing the superior stability of Pt_5La alloy. Detailed inspection of the electrochemical data summarized in Figs. 5(d) and 5(e) confirmed that after 30,000 cycles, there is only a negligible negative shift of 1 mV in the half-wave potential for Pt_5La. While for commercial Pt/C-JM, the half-wave potential directly experienced a large negative shift of 48 mV. And for our catalyst, mass activity decayed from 0.49 to 0.46 A·mg$_{Pt}^{-1}$ after 30,000 cycles with a drop of only 6.1%, proving the great superiority compared to commercial Pt/C-JM (loss nearly 70% mass activity).

Direct insights into high stability of Pt_5La alloy could be observed from Figs. 5(b) and 5(c). First, the CVs before and after the AST test own a high degree of overlap, especially in the characteristic adsorption range of 0.1–0.4 V, indicating that the Pt surface is stable and not prone to remodeling. Also, from Fig. 5(c), the reduction potentials of Pt in the Pt_5La alloy and commercial Pt/C-JM are 0.84 and 0.8 V, respectively. The positive shift indicates that the adsorption of OH in the alloy is weakened and the key intermediate Pt–OH [24, 25] for Pt dissolution did not tend to form and stay, which results in a dual increase in activity and stability. Such electrochemical observation correlated well with the electron transfer observed in XPS and EXAFS in Fig. 3, where electron transfer from La to Pt leads to an increase in the electron cloud density of Pt, as well as a weakened surface adsorption strength of OH species. Comparing the TEM images before and after the stability test in Fig. S5 in the ESM, no obvious change in the morphology of the catalyst was found. In contrast, the ECSA of commercial Pt/C undergoes a significant decay after 30k AST tests from CV curves in Fig. S8 in the ESM, indicating that the reason for the inability to maintain high activity for Pt/C-JM is mainly due to the easy dissolution of Pt and the loss of ECSA caused by re-polymerization. Additionally, we also performed XPS delectation of Pt 4f spectrum after the stability test. Compared with commercial Pt/C-JM, it is found that metallic Pt(0) and Pt(II) oxide in Pt_5La alloy both maintained negative shift after electrochemical testing in Fig. S6 in the ESM, indicating that strong binding interaction still exists, and that is the origin of high stability. To here, the intrinsic stability of Pt_5La has been elucidated from both the electrochemical evidence and the electronic state delectation.

3 Conclusions

In this work, we have created a simple and feasible synthesis method of intermetallic alloys between rare earth metal and

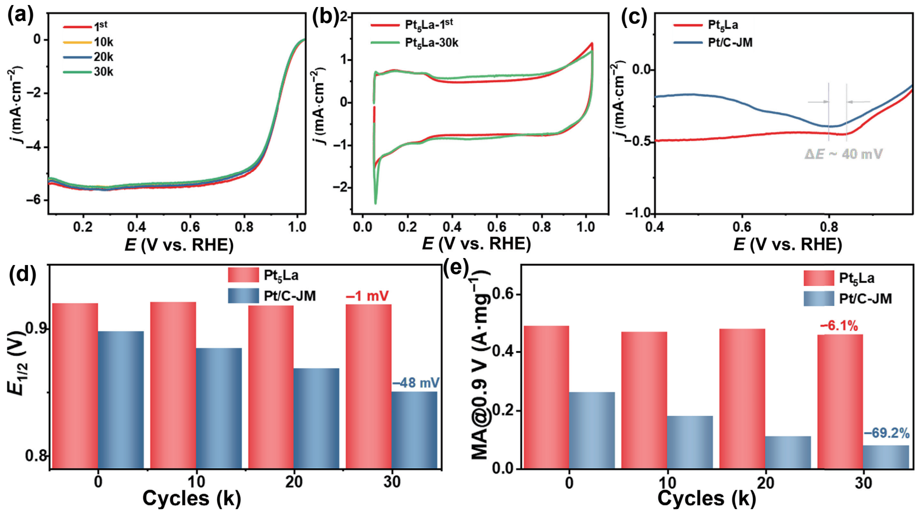

Figure 5 (a) LSV curves of Pt_5La before and after 10k, 20k, and 30k cycling in AST test. (b) Comparison of CV curves in N_2-saturated electrolyte. (c) Comparison of reduction peak potentials of Pt between Pt_5La and Pt/C-JM. (d) Changes of half wave before and after 10k, 20k, and 30k cycling in AST. (e) Changes of mass activity before and after 10k, 20k, and 30k cycling in AST.

platinum with a large-scale discrepancy in standard reduction potential and successfully engaged La into Pt lattice through an atomically dispersed precursor-assisted synthesis method. The formation of Pt_5La alloy was confirmed by a series of characterizations and the available catalyst presented superior activity with the half wave potential of 0.92 V and mass activity of 0.49 $A \cdot mg_{Pt}^{-1}$. Notably, AST data further demonstrate the validity of our approach to deriving highly stable Pt based alloy for electrochemistry by embedding rare earth metal to sublayers. There is a strong charge transfer from La to Pt atoms in the alloy NCs, which significantly changes the electronic structure of Pt and further triggers decrease in adsorption strength of the adsorbed species. Such interaction, evidenced by electrochemical reduction peak of Pt, not only ensures high activity for ORR but also plays a major role in improving stability.

Acknowledgements

The work was supported by National Key R&D Program of China (No. 2021YFA1501101), the National Natural Science Foundation of China (Nos. 21875243, 21673220, 21733004, and U1601211), the Jilin Province Science and Technology Development Program (Nos. 20190201270JC, 20180101030JC, and 20200201001JC), Dalian National Laboratory for Clean Energy (DNL), Chinese Academy of Sciences (CAS), and the Research Innovation Fund (No. DNL202010).

Electronic Supplementary Material: Supplementary material (detailed experimental procedures, TEM images of Pt_5La, XPS spectra, and comparison of morphology of catalysts before and after AST teats by TEM) is available in the online version of this article at https://doi.org/10.1007/s12274-022-4868-3.

References

[1] Zhang, J. W.; Yuan, Y. L.; Gao, L.; Zeng, G. M.; Li, M. F.; Huang, H. W. Stabilizing Pt-based electrocatalysts for oxygen reduction reaction: Fundamental understanding and design strategies. *Adv. Mater.* **2021**, *33*, 2006494.

[2] Kodama, K.; Nagai, T.; Kuwaki, A.; Jinnouchi, R.; Morimoto, Y. Challenges in applying highly active Pt-based nanostructured catalysts for oxygen reduction reactions to fuel cell vehicles. *Nat. Nanotechnol.* **2021**, *16*, 140–147.

[3] Luo, L. X.; Fu, C. H.; Wu, A. M.; Zhuang, Z. C.; Zhu, F. J.; Jiang, F. L.; Shen, S. Y.; Cai, X. Y.; Kang, Q.; Zheng, Z. F. et al. Hydrogen-assisted scalable preparation of ultrathin Pt shells onto surfactant-free and uniform Pd nanoparticles for highly efficient oxygen reduction reaction in practical fuel cells. *Nano Res.* **2022**, *15*, 1892–1900.

[4] Fang, D. H.; Wan, L.; Jiang, Q. K.; Zhang, H. J.; Tang, X. J.; Qin, X. P.; Shao, Z. G.; Wei, Z. D. Wavy PtCu alloy nanowire networks with abundant surface defects enhanced oxygen reduction reaction. *Nano Res.* **2019**, *12*, 2766–2773.

[5] Kim, C.; Dionigi, F.; Beermann, V.; Wang, X. L.; Möller, T.; Strasser, P. Alloy nanocatalysts for the electrochemical oxygen reduction (ORR) and the direct electrochemical carbon dioxide reduction reaction (CO_2RR). *Adv. Mater.* **2019**, *31*, 1805617.

[6] Tian, X. L.; Zhao, X.; Su, Y. Q.; Wang, L. J.; Wang, H. M.; Dang, D.; Chi, B.; Liu, H. F.; Hensen, E. J. M.; Lou, X. W. et al. Engineering bunched Pt-Ni alloy nanocages for efficient oxygen reduction in practical fuel cells. *Science* **2019**, *366*, 850–856.

[7] Beermann, V.; Holtz, M. E.; Padgett, E.; De Araujo, J. F.; Muller, D. A.; Strasser, P. Real-time imaging of activation and degradation of carbon supported octahedral Pt-Ni alloy fuel cell catalysts at the nanoscale using *in situ* electrochemical liquid cell STEM. *Energy Environ. Sci.* **2019**, *12*, 2476–2485.

[8] Ze, H.; Chen, X.; Wang, X. T.; Wang, Y. H.; Chen, Q. Q.; Lin, J. S.; Zhang, Y. J.; Zhang, X. G.; Tian, Z. Q.; Li, J. F. Molecular insight of the critical role of Ni in Pt-based nanocatalysts for improving the oxygen reduction reaction probed using an *in situ* SERS borrowing strategy. *J. Am. Chem. Soc.* **2021**, *143*, 1318–1322.

[9] Wu, Z. P.; Caracciolo, D. T.; Maswadeh, Y.; Wen, J. G.; Kong, Z. J.; Shan, S. Y.; Vargas, J. A.; Yan, S.; Hopkins, E.; Park, K. et al. Alloying-realloying enabled high durability for Pt-Pd-3d-transition metal nanoparticle fuel cell catalysts. *Nat. Commun.* **2021**, *12*, 859.

[10] Ao, X.; Zhang, W.; Zhao, B. T.; Ding, Y.; Nam, G.; Soule, L.; Abdelhafiz, A.; Wang, C. D.; Liu, M. L. Atomically dispersed Fe-N-C decorated with Pt-alloy core−shell nanoparticles for improved activity and durability towards oxygen reduction. *Energy Environ. Sci.* **2020**, *13*, 3032–3040.

[11] Huang, L.; Zaman, S.; Tian, X. L.; Wang, Z. T.; Fang, W. S.; Xia, B. Y. Advanced platinum-based oxygen reduction electrocatalysts for fuel cells. *Acc. Chem. Res.* **2021**, *54*, 311–322.

[12] Luo, E. G.; Zhang, H.; Wang, X.; Gao, L. Q.; Gong, L. Y.; Zhao, T.; Jin, Z.; Ge, J. J.; Jiang, Z.; Liu, C. P. et al. Single-atom Cr-N_4 sites designed for durable oxygen reduction catalysis in acid media. *Angew. Chem., Int. Ed.* **2019**, *58*, 12469–12475.

[13] Greeley, J.; Stephens, I. E. L.; Bondarenko, A. S.; Johansson, T. P.; Hansen, H. A.; Jaramillo, T. F.; Rossmeisl, J.; Chorkendorff, I.; Nørskov, J. K. Alloys of platinum and early transition metals as oxygen reduction electrocatalysts. *Nat. Chem.* **2009**, *1*, 552–556.

[14] Ryoo, R.; Kim, J.; Jo, C.; Han, S. W.; Kim, J. C.; Park, H.; Han, J.; Shin, H. S.; Shin, J. W. Rare-earth-platinum alloy nanoparticles in mesoporous zeolite for catalysis. *Nature* **2020**, *585*, 221–224.

[15] Escudero-Escribano, M.; Malacrida, P.; Hansen, M. H.; Vej-Hansen, U. G.; Velázquez-Palenzuela, A.; Tripkovic, V.; Schiøtz, J.; Rossmeisl, J.; Stephens, I. E. L.; Chorkendorff, I. Tuning the activity of Pt alloy electrocatalysts by means of the lanthanide contraction. *Science* **2016**, *352*, 73–76.

[16] Xiang, S.; Wang, L.; Huang, C. C.; Fan, Y. J.; Tang, H. G.; Wei, L.; Sun, S. G. Concave cubic PtLa alloy nanocrystals with high-index facets: Controllable synthesis in deep eutectic solvents and their superior electrocatalytic properties for ethanol oxidation. *J. Power Sources* **2018**, *399*, 422–428.

[17] Borchert, H.; Borchert, Y.; Kaichev, V. V.; Prosvirin, I. P.; Alikina, G. M.; Lukashevich, A. I.; Zaikovskii, V. I.; Moroz, E. M.; Paukshtis, E. A.; Bukhtiyarov, V. I. et al. Nanostructured, Gd-doped ceria promoted by Pt or Pd: Investigation of the electronic and surface structures and relations to chemical properties. *J. Phys. Chem. B* **2005**, *109*, 20077–20086.

[18] Hu, Y.; Jensen, J. O.; Cleemann, L. N.; Brandes, B. A.; Li, Q. F. Synthesis of Pt-rare earth metal nanoalloys. *J. Am. Chem. Soc.* **2020**, *142*, 953–961.

[19] Wang, H. F.; Chen, L. Y.; Pang, H.; Kaskel, S.; Xu, Q. MOF-derived electrocatalysts for oxygen reduction, oxygen evolution and hydrogen evolution reactions. *Chem. Soc. Rev.* **2020**, *49*, 1414–1448.

[20] Chen, H.; Wang, D. L.; Yu, Y. C.; Newton, K. A.; Muller, D. A.; Abruña, H.; Disalvo, F. J. A surfactant-free strategy for synthesizing and processing intermetallic platinum-based nanoparticle catalysts. *J. Am. Chem. Soc.* **2012**, *134*, 18453–18459.

[21] Liang, J. S.; Zhao, Z. L.; Li, N.; Wang, X. M.; Li, S. Z.; Liu, X.; Wang, T. Y.; Lu, G.; Wang, D. L.; Hwang, B. J. et al. Biaxial strains mediated oxygen reduction electrocatalysis on Fenton reaction resistant $L1_0$-PtZn fuel cell cathode. *Adv. Energy Mater.* **2020**, *10*, 2000179.

[22] Hu, Y. Z.; Guo, X. Y.; Shen, T.; Zhu, Y.; Wang, D. L. Hollow porous carbon-confined atomically ordered $PtCo_3$ intermetallics for an efficient oxygen reduction reaction. *ACS Catal.* **2022**, *12*, 5380–5387.

[23] Zhu, S. Y.; Wang, X.; Luo, E. G.; Yang, L. T.; Chu, Y. Y.; Gao, L. Q.; Jin, Z.; Liu, C. P.; Ge, J. J.; Xing, W. Stabilized Pt cluster-based catalysts used as low-loading cathode in proton-exchange membrane fuel cells. *ACS Energy Lett.* **2020**, *5*, 3021–3028.

[24] Rizo, R.; Fernández-Vidal, J.; Hardwick, L. J.; Attard, G. A.; Vidal-Iglesias, F. J.; Climent, V.; Herrero, E.; Feliu, J. M. Investigating the presence of adsorbed species on Pt steps at low potentials. *Nat. Commun.* **2022**, *13*, 2550.

[25] Dong, J. C.; Zhang, X. G.; Briega-Martos, V.; Jin, X.; Yang, J.; Chen, S.; Yang, Z. L.; Wu, D. Y.; Feliu, J. M.; Williams, C. T. et al. *In situ* Raman spectroscopic evidence for oxygen reduction reaction intermediates at platinum single-crystal surfaces. *Nat. Energy* **2019**, *4*, 60–67.